Hierarchically patterned multiphase steels created by localised laser treatments

Breukelman, H. J.; Santofimia, M. J.; Hidalgo, J.

DOI
10.1016/j.matdes.2022.110984

Publication date
2022

Document Version
Final published version

Published in
Materials and Design

Citation (APA)
Breukelman, H. J., Santofimia, M. J., & Hidalgo, J. (2022). Hierarchically patterned multiphase steels created by localised laser treatments. *Materials and Design*, *221*, Article 110984. https://doi.org/10.1016/j.matdes.2022.110984

Materials & Design 221 (2022) 110984

Contents lists available at ScienceDirect

Materials & Design

journal homepage: www.elsevier.com/locate/matdes

Hierarchically patterned multiphase steels created by localised laser treatments

H.J. Breukelman [a], M.J. Santofimia [a], J. Hidalgo [a,b,*]

[a] Department of Materials Science and Engineering, Delft University of Technology, Mekelweg 2, 2628CD Delft, the Netherlands
[b] Universidad de Castilla La Mancha, ETSII-INEI. DYPAM Research Group, Avda. Camilo José Cela s/n, Ciudad Real 13071, Spain

HIGHLIGHTS

- fcc/bcc patterned mesostructures are created by solid-state transformations in a Fe-Ni-C steel through the application of local laser heat treatments.
- The behavior of fcc/bcc mesostructures is controlled by the topology and the martensite strength, which can be tailored through tempering.
- The proposed approach to create patterned mesostructures opens new strategies in the design of steel and other metal alloys.

GRAPHICAL ABSTRACT

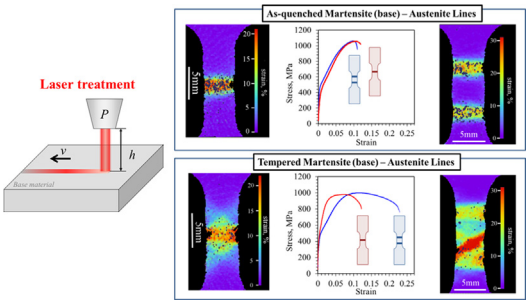

ARTICLE INFO

Article history:
Received 3 May 2022
Revised 18 July 2022
Accepted 22 July 2022
Available online 25 July 2022

Keywords:
Patterned microstructures
Austenite
Martensite
Local heat treatment
Laser material processing
Flash heating

ABSTRACT

The realisation of sophisticated hierarchically patterned multiphase steels has the potential to enable unprecedented properties in engineering components. The present work explores the controlled creation of patterned multiphase steels in which the patterns are defined by two different crystal structures: face centre cubic or fcc (austenite) and body centre cubic or bcc (martensite). These austenite/martensite mesostructures are generated by solid–solid phase transformations during the application of localised laser heat treatments in a Fe-Ni-C alloy. In particular, four patterned configurations are analysed in this work consisting of one or two horizontal austenite line structures imprinted in a base of as-quenched or tempered martensite. Digital image correlation analysis during tensile testing of the developed materials showed that both the strength of the base martensite and the mesostructure at the gauge have a strong effect on the resulting properties. Clear differences were observed among the configurations in strain partitioning, hardening of the different constituents and failure. The uniform elongation and tensile strength are increased with respect to that of the reference martensite and austenite, respectively. Concepts explored in this work can be extended to more complex patterns and other base microstructures, opening novel strategies to engineer properties in steel and other alloys.

1. Introduction

Introducing a hierarchy of topological features into the patterned structure of metamaterials and composites has been credited with improving specific elastic properties, energy absorption and tolerance to damage and can, in exceptional examples, result

* Corresponding author at: Department of Materials Science and Engineering, Delft University of Technology, Mekelweg 2, 2628CD Delft, the Netherlands.
E-mail address: Javier.HidalgoGarcia@uclm.es (J. Hidalgo).

https://doi.org/10.1016/j.matdes.2022.110984
0264-1275/

in unusual properties such as negative stiffness [1,2]. Chiral and anti-chiral hierarchical patterns in honeycombs crucially affect the in-plane mechanical properties of these structures and can lead to an improved and tailored stiffness and shear resistance [3].Playing with pattern topology can lead to composites being able to change their Poisson ratio from positive to negative depending on temperature [4]. Besides, novel algorithms based on the concurrent topological design of multiple phase materials, predict optimum distributions of microstructure constituents in regular patterns to optimise mechanical properties. For example, these algorithms can be applied to maximize the stiffness of macrostructures combining multiple materials [5]. These observations in composite non-metallic materials are sufficiently promising to also consider these novel approaches of mesostructure design in advanced metal alloys.

Indeed, examples of steel composites mesostructured in patterns can be readily found in the literature [6]. These steels commonly exhibit superior properties compared to steels with a monolithic structure. Damascus steel is a historical example of mesostructured material with distinct mechanical properties [7]. Steel composites with different pattern configurations can be created by local carburisation and decarburisation [6,8]. Layered metal composites are another example of simple mesoscale patterns with regions of distinguishably different microstructures that have demonstrated the potential to achieve high strength and ductility, high specific stiffness and high tolerance to damage. An example of a multi-layered Ti-Al composite is provided by Huang *et al.* [9], while Ojima *et al.* [10] developed a multilayer steel composite. Exceptional combinations of strength and ductility can be explained by the presence of multiple deformation mechanisms. They include an effective strain transfer and redistribution of stresses among brittle/ductile layers that relieve strain localisation and result in accommodation of strain and delayed failure of the brittle layer. Mesostructures developed in welds [11,12] and additively manufactured materials [13] exhibit similar mechanisms, and improved properties can be achieved by playing with the mesostructure topology and local microstructures. Further examples can be found in multiphase metals. Zhao *et al.* [14] found that banded bainite/ferrite structures possess better deformation compatibility than equiaxial structures, which results in higher ultimate strength and elongation along the band direction, and Liu *et al.* [15] showed that improved fracture resistance in steels with ultrahigh strength can be achieved by engineering the microstructure in martensite and austenite bands of around 10 μm width. The underlying deformation mechanisms leading to improved properties in these materials are comparable to those described in layered metal mesostructures, which suggests that these mechanisms can be scaled to different dimensions and calls for the design of hierarchical structures to fully benefit from these mechanisms.

The capacity for complex microstructures in Fe-C systems, which develop based on the thermomechanical history and can be tailored by heat treatments, offers possibilities for patterned microstructures. Creating these patterns on a local scale is possible using laser heat treatments. The use of lasers as a heat source to modify the microstructure by solid-state phase transformations of the near-surface regions of materials is a well-established technology [16,17]. Some examples of laser treatments include surface hardening or softening to improve wear resistance, fracture toughness or machinability. Syed *et al.* [18] accomplished surface hardening by the formation of martensite after applying a laser treatment over a ferritic steel base material. Lenuda *et al.* [19] exploited secondary hardening during the tempering of tool steel by a laser source. Telranhdhe et al. [20], on the contrary, made use of laser surface treatments to soften the microstructure and thus improve the machinability of Ti alloys. In all these processes, a homogenous microstructure is developed along the material surface and microstructure varies only in the direction of the material bulk. These studies demonstrate the suitability of using laser treatments to engineer the microstructure of alloys, although the use of this technology to develop pattern topologies with the potential to achieve unprecedented properties has been barely explored. Only very recently, Andreev *et al.* [21] and Pimenov [22] developed gradient microstructures in a Fe-Cr-Ni metastable austenitic steel by reverting a cold-rolled martensitic microstructure by laser treatment using shadow masks of different geometries.

In the present work, hierarchical patterned austenite/martensite structures are created by localised laser heat treatments in a Fe-Ni-C alloy. Austenitic lines are imprinted over two different martensitic microstructures with different strengths to investigate the effect of the martensite strength on the resulting mechanical properties of the patterned material. In a previous work [23], it was demonstrated that the strength ratio between austenite and martensite controls the strength and ductility in advanced steels. Here, this concept is further investigated using the mesostructured steels created by the present approach.

2. Materials and methods

2.1. Material and specimens preparation

Fig. 1 outlines the complete approach followed to create the hierarchically patterned steels. (1) First, a preliminary heat treatment is applied to the steel exhibiting a metastable austenite microstructure at room temperature, T_{room}. (2) Thereafter the steel is subjected to a cryogenic treatment to temperatures below its martensitic start temperature, *MS*, to create a martensitic base microstructure. In a subgroup of samples, this is followed by a tempering treatment. (3) In the last step, the laser treatment is conducted to locally raise the temperature of the material to a temperature sufficiently high to revert the microstructure into austenite, thus creating mesoscale features whose extent and microstructure are controlled by the laser process parameters, and can be built into patterns.

Four pattern configurations are analysed in this work consisting of one (–) or two (=) horizontal austenite lines imprinted in as-quenched (M) or tempered (T) base materials perpendicular to the major axis of the tensile specimen as schematised in Fig. 1a. The resulting microstructures will be denominated as M/A if formed by quenched martensite and austenite, and as T/A if formed by tempered martensite and austenite. Including the indication of the number of imprinted austenite lines, four specimens with the following shorthand notation are created: 1) M/A –, 2) M/A =, 3) T/A – and 4) T/A =. The geometry of the lines is such that the single line is imprinted in the middle of the gauge of a tensile specimen, whereas the two lines are separated approximately 4 mm, either line being equidistant from the centre of the gauge and separated by a martensitic region. The present geometries were chosen such that isostress conditions hold for the uniform elongation domain of the tensile testing, facilitating the interpretation. The selected base materials allow for varying the strength ratio between austenite and martensite phases.

Metastable austenitic steel with a composition of 0.2C-25Ni-0.02Mn (wt. %) is selected for the study. The MS is estimated at 292 K by thermodynamical calculations using JMatPro software, though dilatometry experiments revealed that *MS* temperature might be slightly below this temperature. The alloy was vacuum cast in an 80 mm × 80 mm × 400 mm billet that was subsequently forged to a 50 mm × 50 mm × 1000 mm billet and homogenised at 1273 K for 12 h. Uniaxial tensile test specimens with dimensions shown in Fig. 1b were machined from the billet. All machined specimens were subjected to an alkali chloride salt bath treatment at

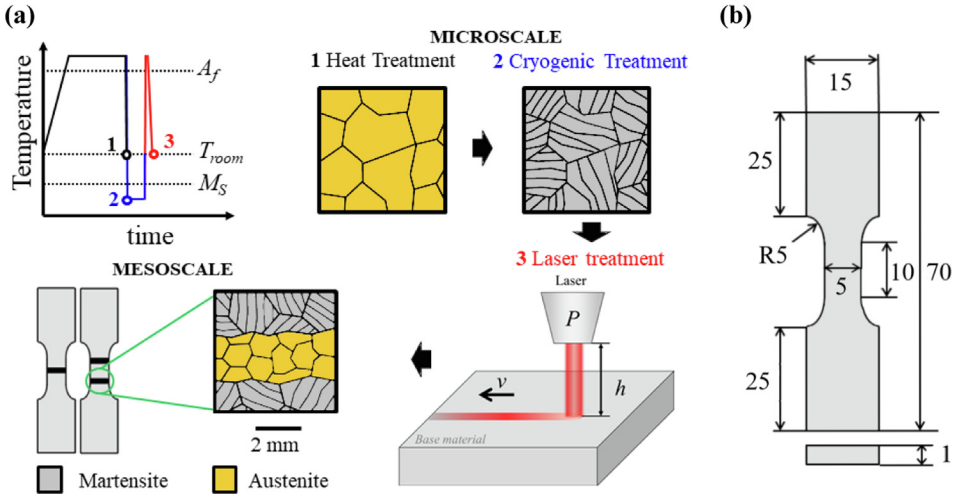

Fig. 1. (a) Scheme of the different steps for creating austenite/martensite patterned structures by localised laser treatments. The temperature variation with time and the characteristic microstructure after every step are represented. This scheme can be applied to any austenitic steel exhibiting an M_S below room temperature. (b) Dimensions of the tensile specimens in mm.

1200 K during 600 s to develop an austenitic microstructure. Thereafter, specimens were immersed in liquid nitrogen (77 K) for 300 s to obtain a fully martensitic base microstructure. Some as-quenched specimens were tempered at 523 K in a sodium nitride salt bath for half an hour, which is far below the 713 K austenite starting temperature for this alloy. The use of salt baths in annealing and tempering treatments enabled precise control of the objective temperatures during heat treatment. Besides, the molten salts act as a protective media to prevent oxidation and decarburization.

A Trumpf HL3006D Nd:YAG laser with a continuous wave pulse at a wavelength of 1064 nm and a focal length of 170 mm was used for the localised laser treatments. The power distribution of the laser beam is assumed close to a Gaussian distribution. A shielding argon atmosphere is used to prevent oxidation of the surface of the specimen. Specimens' surfaces were ground up to a P80 sandpaper grit finish to mitigate the risk of specular reflection of laser radiation. The schematic of the experimental setting is shown in Fig. 1. The power of the laser, *P*, the speed of the flat coupon, *v*, and the focal-spot diameter of the laser, were adjusted by a design of experiments to 400 W, 25 mm/s and 0.78 mm respectively to obtain full austenitisation through the specimen thickness and avoiding melting.

2.2. Microstructure characterisation

Specimens were metallographically prepared by grinding and polishing to 1 μm diamond paste for microstructure characterisation. To reveal the austenitic microstructure, the specimens were etched with waterless Kalling's #2 reagent (5 g $CuCl_2$ + 100 ml of HCl at 33 % + 100 ml Ethyl alcohol). Nital 2 % etching was used to reveal the martensitic microstructure. Light optical microscopy (LOM) was performed using a Leica DMLM and a Keyence VHX-100 digital microscope. A JEOL JSM-6500F scanning electron microscope (SEM) in secondary electron imagining detection mode was used for a detailed characterisation of the microstructures.

To determine the retained austenite fraction after the cryogenic treatment, X-ray diffraction measurements were carried out in a Bruker D8 Advance diffractometer in Bragg-Brentano geometry with a graphite monochromator and Vantec position-sensitive detector. Cobalt radiation was used to obtain a diffractogram covering 20° – 135° with a step size of 0.021° 2θ and counting time per step of 2 s. This range cover the peaks {111}, {200}, {220}, {311} and {222} for austenite and {110}, {200}, {211} and {220} for martensite. Crystalline phases were indexed using standard X-ray diffraction patterns acquired from the International Centre for Diffraction Data (ICDD) [24]. Phase quantification was performed through Rietveld refinement by using MAUD software [25].

2.3. Mechanical characterisation

Hardness Vickers HV0.2 of the base materials and the four pattern configurations at different zones were measured in an EMCO G5 DuraScan. Uniaxial tensile tests were performed in an Instron 5500R device, using a 100 kN load cell. An extensometer of 7.5 mm gauge length was used to measure the strain. To gain insight into the local strain of the specimens, a Limess Q400 digital image correlation (DIC) camera was used. The surface of the specimens was first painted white and sprayed with black paint to create contrasting speckles for the DIC measurement. An image was captured every-five seconds during the test, which corresponds to a picture of every 0.003 strain increment. Complementary to the extensometer, the strain is measured with DIC data. In lasered specimens, the strain is measured relative to an initial length that approximately covers half of the austenite and half of the martensite microstructure in the top surface of the laser-affected zone (LAZ).

3. Results

3.1. Microstructure characterisation

Fig. 2a shows a micrograph of the initial austenitic microstructure at room temperature. An average austenite grain size of 72 ± 4 μm was obtained after the analysis of more than 100 grains by ImageJ software [26]. A large population of twins is observed in the microstructure. Martensite formation is present close to the specimen's surface, as shown in Fig. 2b, leading to a volume fraction of 0.3 as measured by XRD at the specimen's surface. The extension in depth of the martensitic region is around 50 μm on average. The presence of martensite at the specimen's surface can be explained by a reduction of constraining hydrostatic pressure at the free surface, which can increase the M_S temperature up to 100 K in steel [27].

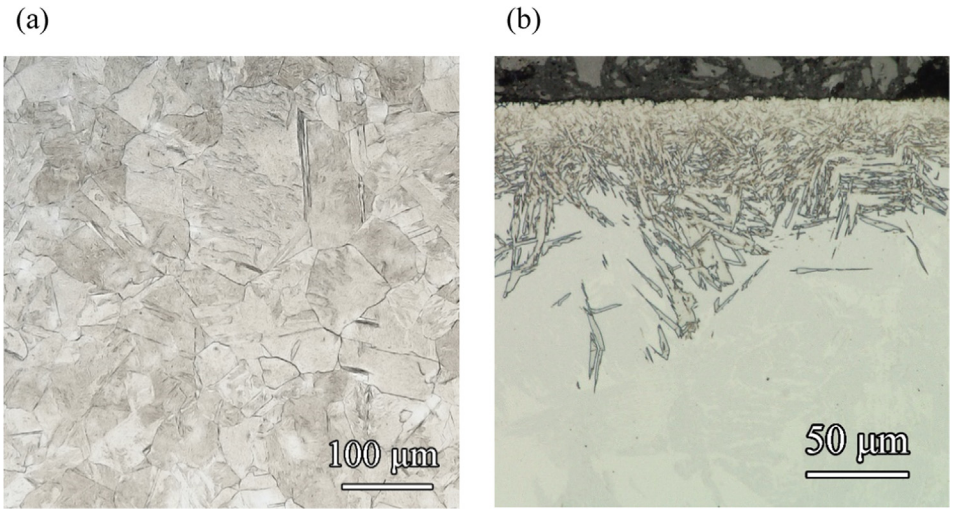

Fig. 2. LOM micrographs at (a) the core (etched with Kalling's reagent) and (b) close to the surfaces of the austenite base material (etched with nital).

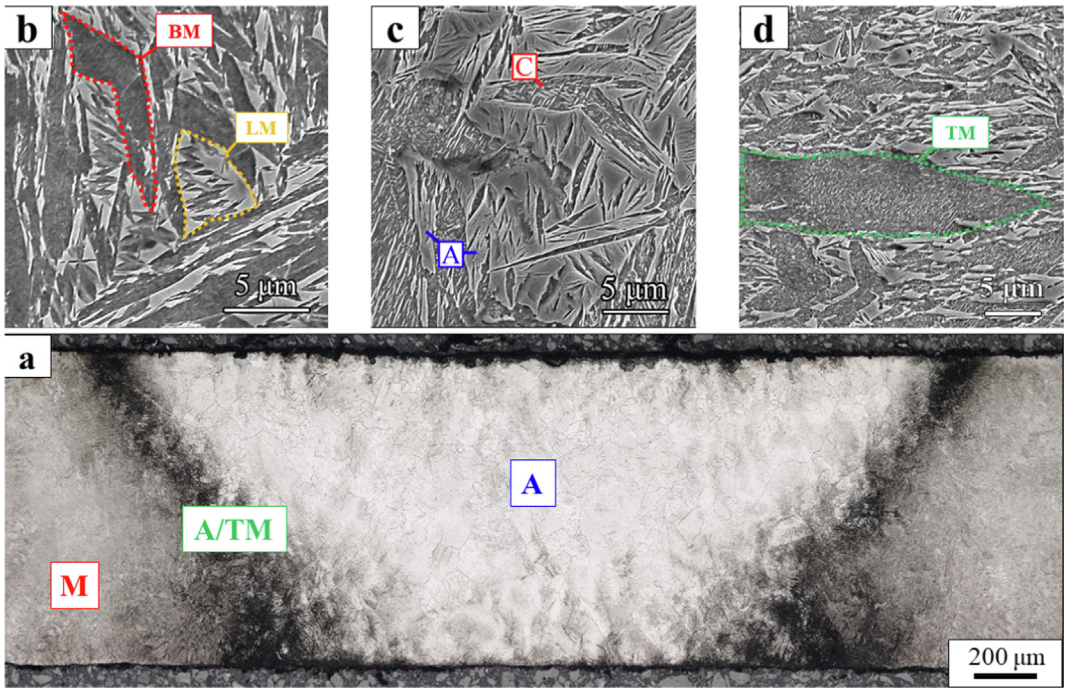

Fig. 3. (a) Cross section of the laser affected zone in martensite one line base material. (b)(c)(d) Magnified SEM micrographs of (b) Martensite base microstructure, (c) A/TM region in (a), and (d) tempered martensite microstructures. M = martensite, TM = tempered martensite, BM = butterfly martensite, LM = lenticular martensite, A = austenite, C = carbides.

Fig. 3b shows a magnified SEM micrograph of the (cryogenically) quenched microstructure, in which butterfly (BM) and lenticular (LM) martensite can be observed. Carbides are not distinguished in martensite at this magnification. In the case of the tempered specimen (Fig. 3d), the martensitic microstructure shows a smoothed shape and fine carbides are spotted inside. Some austenite seems to be observed in Fig. 3 b and d, in both as-quenched and tempered martensite. XRD analysis revealed a 0.08 ± 0.01 fraction of austenite in these microstructures.

Fig. 3a shows the cross-section of the laser affected zone (LAZ) corresponding to a laser line imprinted in an as-quenched specimen. Similar features are observed in the LAZ present at the laser line imprinted in the tempered specimens. A microstructural gradient is observed, developing radially from the laser contact area at the surface. This gradient develops due to the rapid and limited total heat input, and swift dissipation of the laser heat, which causes a large thermal gradient. Within the LAZ, two main domains are distinguished: A fully austenitic region (A) with a width of 2400 μm (lasered side of coupon) to 1100 μm (far side), and a dark-etched interface composed of austenite and tempered martensite (A/TM) between this zone and the base microstructure. Regions far from the laser beam are barely heated and thus keep the microstructure of the base material.

The average grain size of austenite in the interior bulk is 103 ± 2 μm. Fine grains of 26 ± 4 μm are observed at the surface in and adjacent to the laser impingement area. These fine grains extend 200 μm to the bulk. Martensite is observed at the surface of the LAZ, but to a lesser extent than in the base austenite speci-

men. A magnified image at the interface region between the base martensitic microstructure and austenite in Fig. 3c reveals a complex microstructure with coarse needle-type carbides in the tempered martensite and large austenite blocks.

3.2. Mechanical characterisation

The hardness Vickers $HV_{0.2}$ of the initial austenitic, martensitic and tempered martensitic microstructures are 212 ± 15, 387 ± 10 and 353 ± 12, respectively. The average hardness in the austenite region at LAZ is 265 ± 25 HV in M/A specimens and 251 ± 21 HV in T/A specimens, which is significantly higher than that for initial austenitic microstructure. In all the conditions, the hardness progressively decreased from the base material region to the centre of the austenite region. This difference in strength is expected to play a role in the deformation behaviour of the composite materials.

In Fig. 4, the uniaxial tensile stress–strain curves of lasered specimens are compared to their corresponding martensite and austenite base materials. The as-quenched martensite base specimen exhibits the highest yield strength (YS) and ultimate tensile strength (UTS) of all base materials. Tempered martensite has a lower YS and UTS and uniform elongation (UE) but higher elongation to break (TE) than as-quenched martensite. The YS of the austenitic specimen is significantly lower than that of both martensitic base microstructures. However, austenite shows a continuous hardening following a linear fashion and reaches a UTS close to that of tempered martensite at a UE that substantially exceeds that of martensite.

The linear hardening in the austenite is associated with mechanically-induced transformation into martensite. Fig. 5a shows the results of austenite fraction measurement with XRD on a single specimen subjected to interrupted tensile testing at different strain levels. Austenite fraction proportionally decreases with strain following a linear trend. An overall decrease of austenite fraction over the course of this test by 0.59 corresponds to a total work hardening of 541 MPa. When most of the austenite is transformed into martensite, the specimen breaks without necking. A linear hardening behaviour is typically observed in austenitic stainless steels that exhibit, among other mechanisms, mechanical induced martensite formation [28]. In some steel grades, a plateau with barely any hardening occurs when UTS and UE are approached, however, deformation is very limited in these materials after UTS.

Fig. 5b shows the development of local strains at the gauge of austenite specimen measured by DIC analysis at 0.2 strain. The strain is homogenous within the tensile specimen gauge reaching local values equivalent to that recorded by an extensometer, which serves as a validation of the uniform strain obtained by DIC. Black dots are a consequence of the development of surface roughness and change in the thickness of the specimens at high stains, which hinders the determination of the local strain by the DIC algorithm.

Focusing on the lasered specimen tensile curves, M/A – and M/A = specimens exhibit a similar work hardening behaviour and their tensile properties seem to approximate an average between the properties of the martensite and austenite base specimens. T/A – and T/A = have similar YS and UTS, which are also comparable to that of M/A specimens. On the contrary, the UE of T/A – is the lowest of all lasered specimens, whereas the UE of T/A = is the highest. The elongation to break of T/A = exceeds that of tempered martensite and is similar to that obtained in the austenitic specimen. In all the configurations, the UE of the lasered specimens is higher than that of the base martensitic microstructures. Tempered lasered configurations show a UTS comparable to the base material. However, different work hardening behaviours are observed.

4. Discussion

Fig. 4 shows that steel properties can be engineered by playing with its mesostructured topology and the strength ratio between austenite and martensite constituting the patterns. Austenite and martensite will strain and harden differently due to their difference in nature and strength. Besides austenite can also suffer a mechanical induced transformation, which will locally alter the strength of the austenite region. Hence, the deformation behaviour in the present patterned steels is controlled by an evolving strain and stress partitioning in what can be simplified at the macroscale to a three-phase system composed of martensite with a controlled degree of tempering, austenite and mechanically formed fresh martensite within LAZ. This is analysed and discussed next comparing the deformation behaviour of individual phases in the laser specimens by DIC experiments. To facilitate the analysis, Fig. 6 shows YS, UTS, UE and TE measured at different zones of the lasered specimens, i.e. for individual phases, together with measurements of reference A, M and T microstructures and measurements obtained from tensile curves of lasered specimens in Fig. 5.

5. Specimens with one imprinted line

Fig. 7 a and c show the macroscopic stress versus strain of individual martensite and austenite phases. The curves are obtained by averaging DIC measurements along the lines shown in the sche-

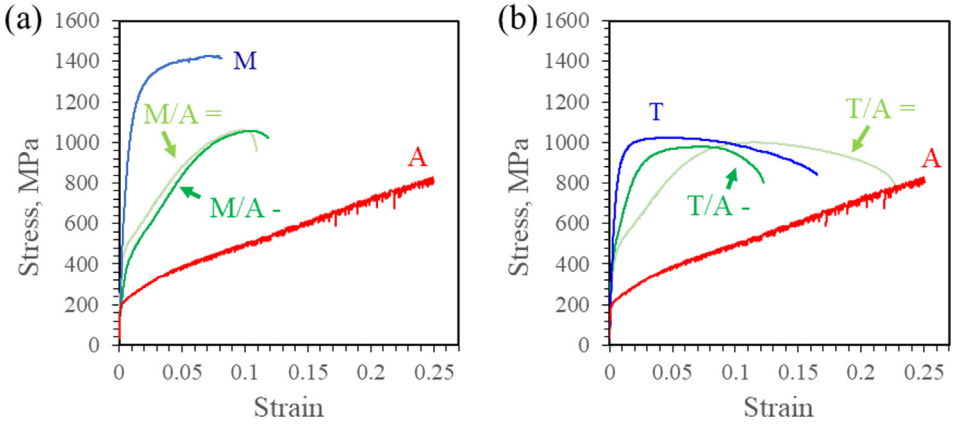

Fig. 4. Comparative uniaxial engineering tensile strain–stress curves of base materials and lasered specimens. (a) A: initial austenite; M: cryogenically quenched martensite; M/A – (one laser line) and M/A = (two laser lines). (b) A: initial austenite; T: tempered martensite; T/A – (one laser line) and line T/A = (two laser lines).

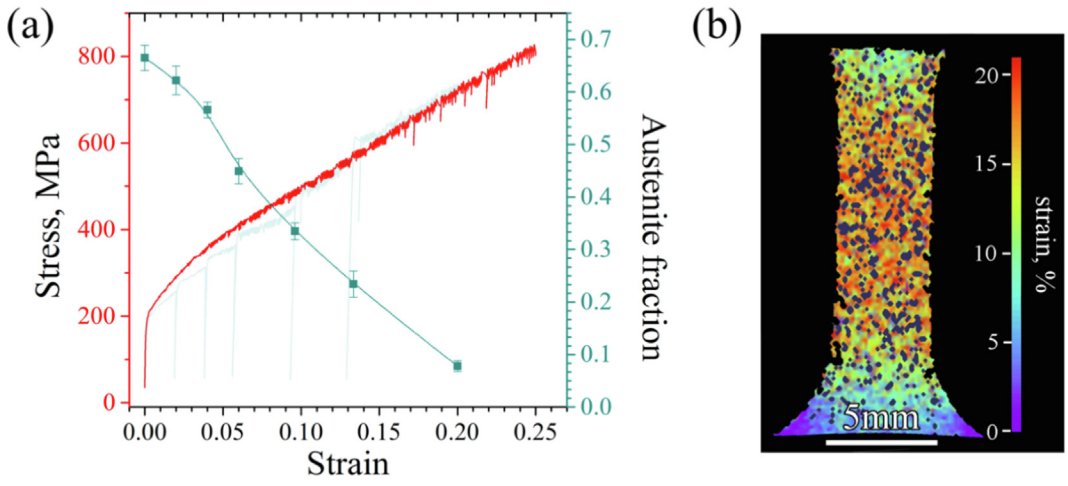

Fig. 5. (a) Engineering stress–strain curve of austenite (in red) represented along with the phase fraction of austenite with strain (green solid symbols) The line present in the figure is presented purely as a reading guide and does not imply a precise fit. The light green stress–strain curve corresponds to the interrupted tests at different strains for XRD measurements. (b) Local strain along the tensile test specimen gauge of the austenite base specimen for a frame of digital image correlation corresponding with 0.2 strain.

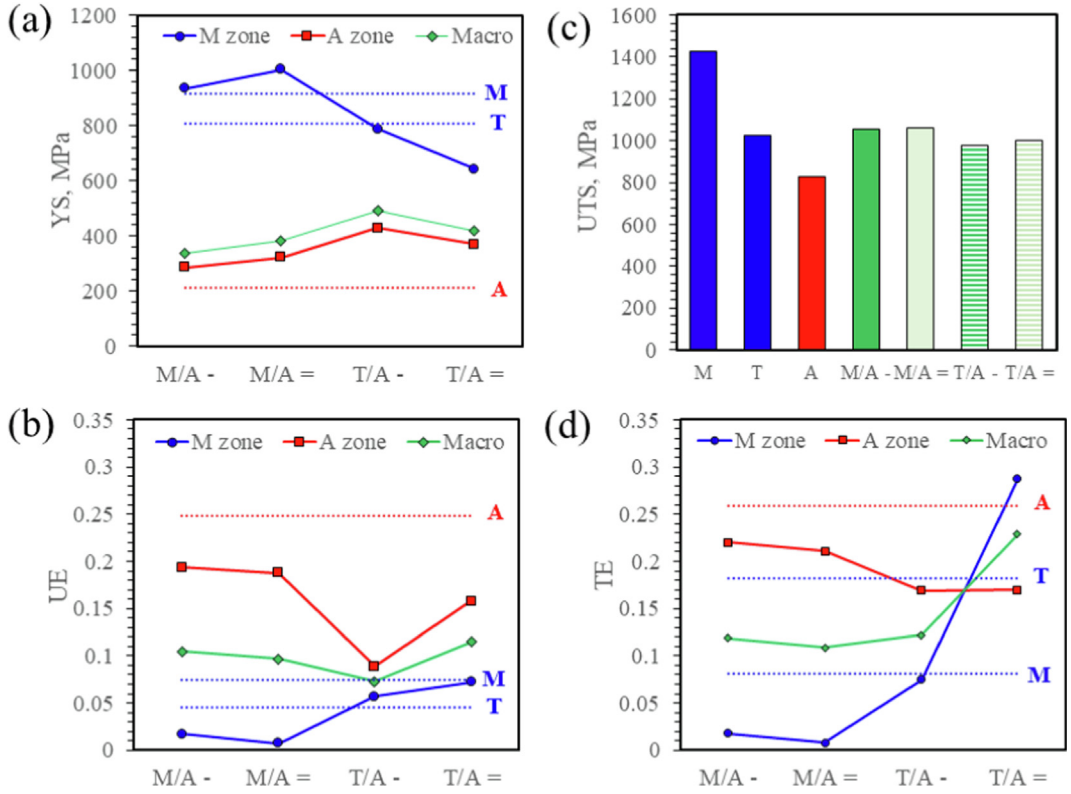

Fig. 6. Comparative mechanical properties of different specimens (Macro) with that measure for individual phases at austenite (A_{zone}) and martensite (M_{zone}) zones by DIC. (a) Yield strength (YS), (b) uniform elongation (UE), (c) ultimate tensile strength (UTS) and (d) total elongation (TE). Dashed lines represent the properties of reference austenite (A), martensite (M) and tempered martensite (T).

matic tensile specimen, in M/A – and T/A – configurations. In supplementary Figure S1, the behaviour of individual phases is compared to that of the composite material. The uniform elongation interval is highlighted by dark colours in the uniaxial strain–stress curves of Fig. 7 a and c.

Since the austenite and martensite bands are arranged perpendicular to the load direction, an isostress condition is assumed reasonable for the analysis until UE. However, a more complex stress state is likely developed at the material bulk resulting from a curved interface between austenite and martensite regions. Isostress cannot be longer assumed from UTS onward and the extended stress–strain curve from UTS/UE to break is presented in light colours, denoting that the assumed stress on this part of the curve is unlikely to represent the actual stress state in the specific phase. The local strains parallel to the load direction at UTS are also shown in Fig. 7 b and d.

At low strains in the elastic regime, austenite and martensite deform equally with increasing stress. Goldman and Robertson

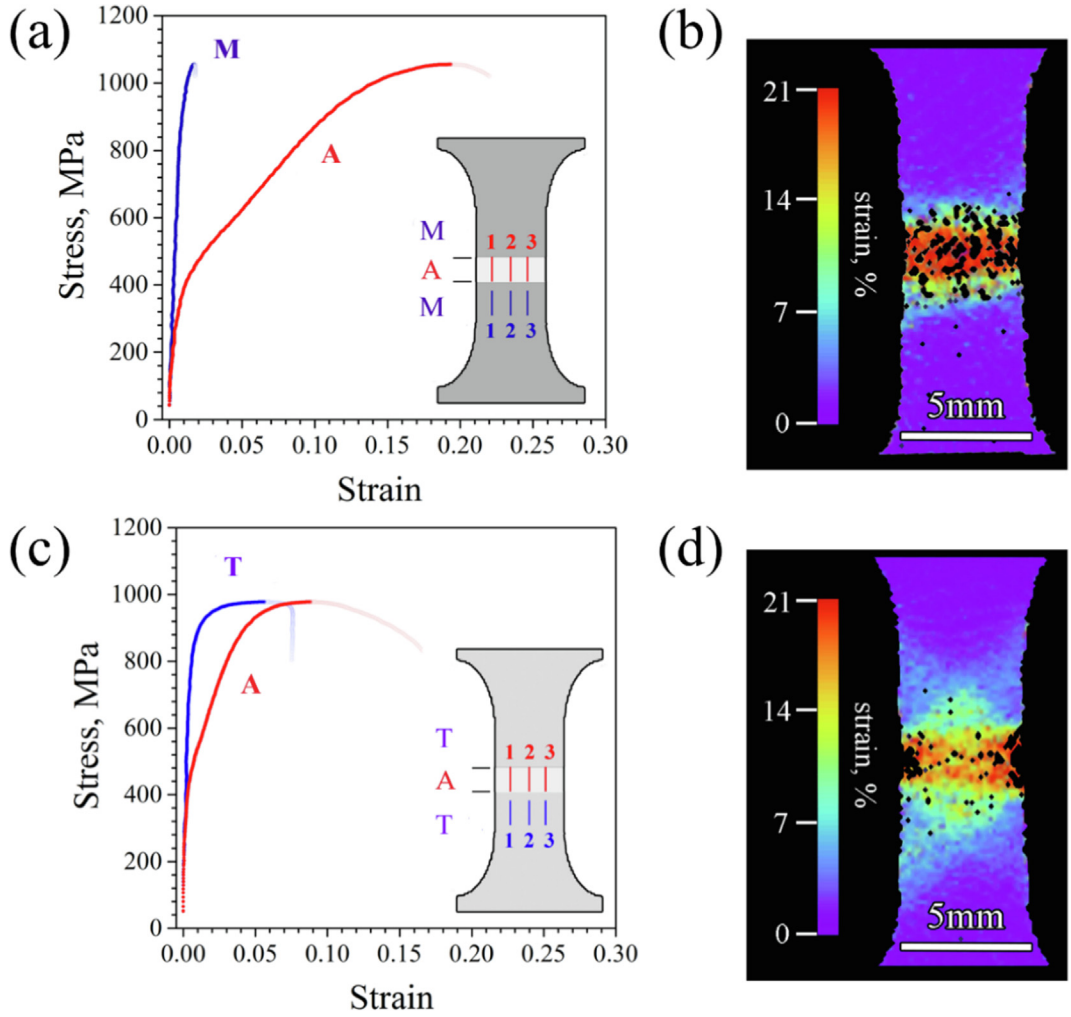

Fig. 7. Engineering stress–strain curves of austenite (A_{zone}) and martensite (M_{zone} and T_{zone}) for (a) M/A – (c) T/A – specimens. The curves were calculated by averaging the strains measured along 3 lines at different zones of the gauge as schematised in the figures. (b) and (d) show local strains developed along the tensile specimen gauge for M/A – and T/A – specimens, respectively, for the frame of digital image correlation corresponding to the UTS.

[29] reported that for a Fe-25Ni-0.6c alloy, the difference between the elastic modulus of austenite and martensite is remarkable in a broad temperature range. However, in the elastic regime of both phases, the difference in deformation between phases for an increment of the applied stress is not as evident as that occurring when one of the phases yields and its secant modulus suddenly drops. At this point, the strain partitioning becomes distinguishable in the curves. Austenite yields first at stress significantly higher than that measured in the fully austenitic specimen, while untempered and tempered martensite yield at a stress equivalent to their corresponding fully martensitic specimens (see Fig. 6a). The high austenite yield stress in lasered specimens is in agreement with its high hardness compared to the reference austenite microstructure. Considering the austenite grain size is equivalent in all conditions, this rise in YS and hardness might be explained by an increase in dislocation density inherited from martensite due to the flash heating and rapid formation of austenite during the laser treatment [30]. This hypothesis is supported by the observation that austenite in M/A, formed from a high dislocation density martensite, has a higher hardness than that of austenite in the T/A specimen, formed from tempered martensite. However, austenite YS in T/A is higher than that in the M/A specimen, which is contradictory to the hardness values. This suggests that additional factors are influencing the YS of the austenite at LAZ, possibly the differences in strength ratio between austenite and martensite in M/A and T/A as well as in the austenite mechanical stability. Further investigations are ongoing to clarify the origin of these observations, though the proposed mechanisms have been observed in advanced steels with austenite/martensite microstructures [23].

Composite material yielding is well linked to the austenite yielding in M/A – and T/A –. From the yield stress, strain partitioning between austenite and martensite is observed. The LAZ, initially composed of austenite and thus referred to as A_{zone}, accommodates most of the plastic strain in M/A – until the break. Martensite zone (M_{zone}) barely deforms in M/A –. In contrast, tempered martensite in T/A – (T_{zone}) takes part of the plastic strain before reaching the UTS. Once the UTS is reached, although T_{zone} keeps deforming, A_{zone} takes most of the deformation until the break. The differences observed in local deformation of these two conditions should be explained by the evolution of hardening of different phases in the composite material and the formation of mechanically induced martensite with increasing macroscopic strains.

The work hardening of A_{zone} follows a linear trend in M/A – and T/A – configurations, which is a consequence of the austenite to martensite mechanical induced transformation. Austenite decomposition increases the work hardening by the formation of strong martensite and also provides extra deformation due to the volume

expansion accompanying the transformation. The total work hardening provided by austenite in all configurations is equivalent to that measured in the reference austenitic specimen. The equivalent total work hardening in the lasered specimens, and the generally high YS of the A_{zones}, therefore, result in improved UTS for all A_{zones} and explain why the UTS of the lasered specimens is broadly similar. However, the work hardening rate of austenite is high in lasered specimens compared to reference austenite, which suggests that the austenite decomposition rate is also high. This leads to a decrease in the UE of austenite compared to reference austenite. Stress equally develops in austenite and martensite in lasered specimens before UTS considering the isostress condition. The high hardening of martensite in composite materials results in a concurrent stress–strain increase in austenite, which explains the high austenite decomposition rate. The austenite UE is particularly low in T/A –, 2.5 times lower than that of the reference austenite specimen and two times lower than that measured in as-quenched martensite and T/A = counterparts (Fig. 6b). In thin interlayer welds combining strong/weak materials, the transverse contraction and development of shear stress in the weak material is restricted by constraining triaxial stress provided by the strong material [11,31]. Hence, the effective (or von Mises) stress is decreased in the interlayer, which inhibits the initiation and development of plastic flow. Lasered lines in the present work can be considered an equivalent case, where the LAZ can be considered the 'weak' interlayer weld. In Fig. 7d, it can be observed that strain concentrates in T_{zone} forming a triangle with a 50–55° angle from the specimen axis, which indicates shear deformation. This behaviour is not observed in M/A –. The high austenite decomposition rate in T/A – can be explained by a less effective restriction of shear stresses in A_{zone} compared to that in M/A –, although a detailed analysis should be done to confirm this hypothesis.

The UTS is dictated by the austenite at LAZ. In M/A –, UTS of A_{zone} is lower than that of martensite in M_{zone}, i.e. base as-quenched martensite. Necking develops at A_{zone} and stresses concentrate in this region, which limits the ability of the martensite to contribute to hardening. The UTS of tempered martensite is comparable to that of austenite in T/A – and part of the strain is accommodated by T_{zone} at stresses near the UTS. Hence, tempered martensite contributes more effectively to the hardening of the composite material, 189 MPa, than as-quenched martensite, 119 MPa.

Most of the austenite in A_{zone} is likely decomposed at UTS. Once all austenite is decomposed at UTS, freshly formed martensite keeps accommodating the strain in M/A –, suggesting that its strength is lower than that of strain hardened as-quenched base martensite. However, mechanically induced martensite cannot hold much more straining and failure occurs forthwith after necking. The failure develops along the LAZ and base material interface, which can be explained by the strain difference between microstructures that cause stress concentration at the interface. A similar situation is reached in T/A – after UTS, although A_{zone} exhibits a significant amount of extra elongation before the specimen breaks. As the strain is concentrated at A_{zone} after UTS, the TE of tempered martensite is significantly lower than that of the reference specimen. However, tempered martensite keeps deforming after UTS. Freshly formed martensite in T/A – might have similar strength compared to hardened tempered martensite, which will favour the strain partitioning between both phases. This contributes to an extended elongation of A_{zone}, resulting in an equivalent TE in M/A – and T/A – despite the low UE in T/A –.

6. Specimens with two imprinted lines

The behaviour of martensite and austenite phases in M/A =, as shown in Fig. 8 a & b, resembles the behaviour observed in the M/A – specimen. The YS, UTS, UE and TE of austenite and martensite match closely in both conditions. The strain is fully concentrated in the austenite zones, as shown in Fig. 8 b & d, and necking occurs at either laser line. The fracture surface develops along the LAZ and the base material interface of one of the lines.

Unlike M/A =, austenite and martensite in T/A = exhibit different behaviour than that of its single line counterpart (see Fig. 8 c & d). The low YS of T_{zone} in T/A = might be the result of an extra tempering of martensite, as a consequence of double laser treatments. However, laser heat input will result in temperatures below 200 °C for just a few seconds. Besides, a similar effect should have been observed in M/A =, although YS of M_{zone} is similar in this specimen to that of its single line counterpart. It seems that in T/A specimens there is a topological effect governing the composite material behaviour that is not manifested in M/A specimens. The austenite uniform elongation in T/A = is approximately twice as high as in T/A –. UE of tempered martensite in T/A = is higher than that of the reference specimen and its TE is strikingly superior. All this contributes to the highest UE and TE of all the composite materials.

Tempered martensite helps to accommodate part of the plastic deformation before UTS in T/A specimens. However, the strain partitioning among phases is more effective in T/A = compared to T/A –. This reduces the strain localisation in A_{zone}, which is assumed to contribute to a decrease in the austenite decomposition rate. This is evidenced by a smoothed austenite hardening rate in T/A =, which in turn contributes to an extended UE. However, the martensite strength is still playing a role in austenite mechanical stability as the austenite UE is higher than its M/A counterparts. As previously discussed, this can be explained by a better restriction of shear stresses in A_{zone} of M/A specimens.

From UTS, the strain is constrained to the central gauge area in T/A specimens. The main difference is that this central area is composed of freshly formed martensite in T/A – and tempered martensite in T/A =. The strength of the base tempered martensite and freshly formed martensite is likely similar in both cases, causing a more homogenous distribution of strains between phases and delaying the necking. However, the strain after UTS is preferentially accommodated by the tempered martensite in the central part of the specimen in T/A=, hindering further straining within the LAZs. Strain in tempered martensite is localized firstly at the sides of the T_{zone} square forming a cross (see Fig. 8d) and later at a band with a 50–55° angle from the specimen axis as shown in Fig. 9. Unlike the other composite materials, the specimen fails following this deformation band, which indicates a shearing-type failure typical of ductile steels.

The results observed in lasered specimens might be extrapolated to the microscale in base martensitic microstructures. Disregarding the difference in scale, austenite is typically embedded between martensite laths in advanced multiphase steels [32], which resembles the configurations recreated at the mesoscale in the present study. A considerable fraction of austenite is retained in both as-quenched and tempered martensite. Differences in the martensite strength have been demonstrated to strongly influence the austenite mechanical stability in low carbon steels [23,33]. Strong martensite surrounding retained austenite helps the mechanical stabilisation and contributes to an extended UE. In the present study, the low UE of tempered martensite compared to as-quenched martensite (Fig. 6c) might be explained by the differences in retained austenite stability influenced by the martensite strength. At the macroscopic scale, the composite materials exhibit extended UE compared to martensitic reference materials, likely due to a high austenite fraction. However, the differences in the macroscopic behaviour of composite materials cannot be only explained by austenite mechanical stability controlled by base martensite strength. The topology of phase distribution in the

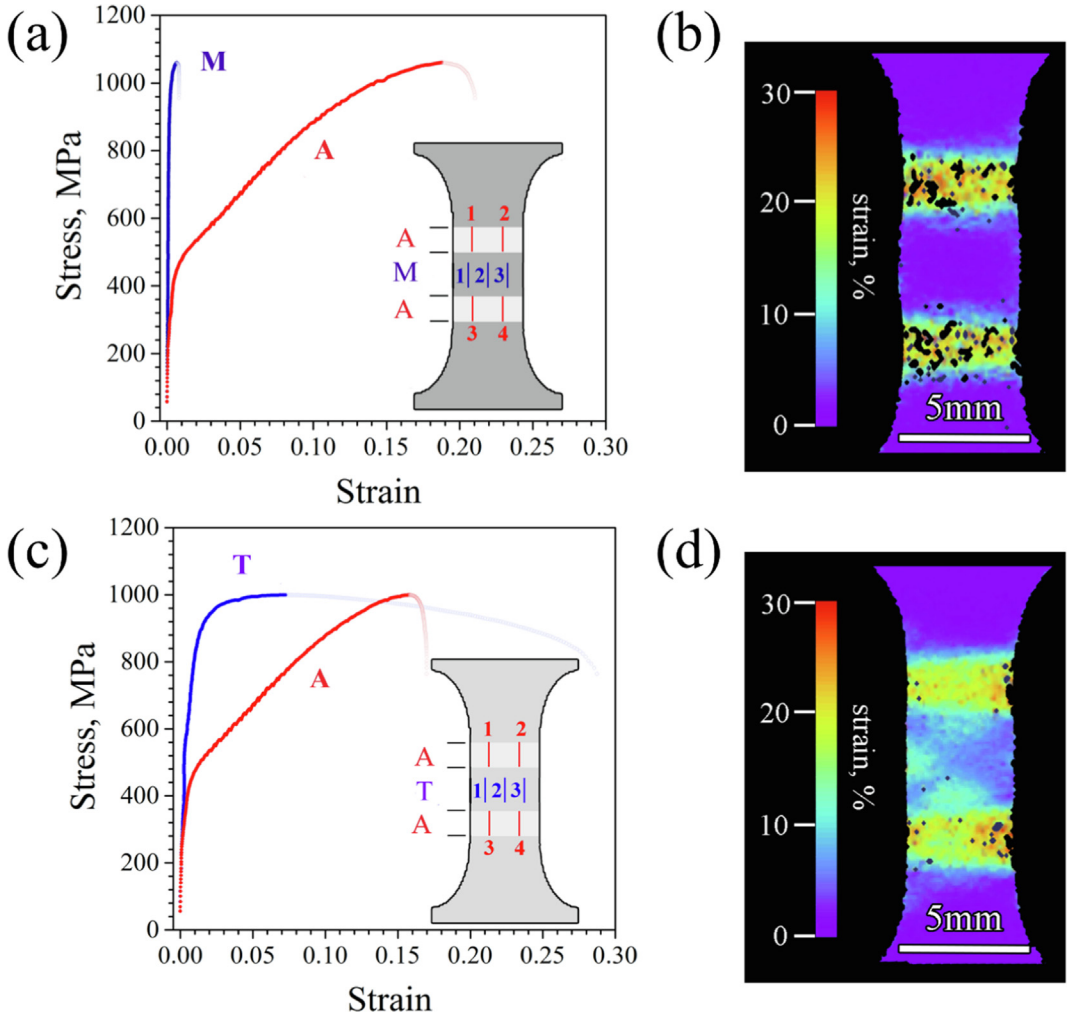

Fig. 8. Engineering stress–strain curves of austenite (A_{zone}) and martensite (M_{zone} and T_{zone}) for (a) M/A – (c) T/A – specimens. The curves were calculated by averaging the strains measured along 3–4 lines at different zones of the gauge as schematised in the figures. (b) and (d) show local strains developed along with the tensile specimen gauge for M/A – and T/A – specimens, respectively, for the frame of digital image correlation corresponding to the UTS.

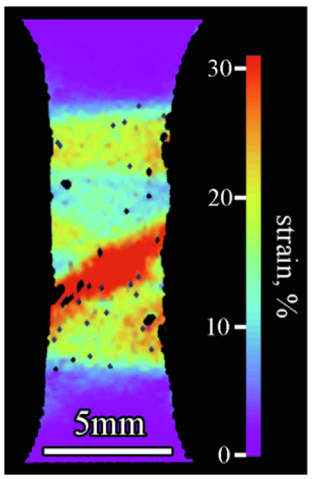

Fig. 9. Local strain in T/A = specimen at 0.2 macroscopic strain, close to breaking.

material is playing an important role, as demonstrated in the present study and other works in literature [9,10,14,15]. In typical steels and multiphase alloys, phases will be sufficiently randomly distributed to comfortably disregard the effect of topology on its mechanical behaviour. However, for a fundamental understanding of microscale effects, studying topology effects by means of mesostructured composites as a proxy for the smaller scale might make a valuable addition to the available research methods.

7. Applicability of mesostructured materials by localised laser treatments

This work presents evidence that patterned steel structures, and thus their deformation mechanisms, can be tailored at different scales (micro and *meso*) by the application of localised laser treatments to different steel base microstructures. These concepts have been demonstrated in model steel, in which a good combination of strength and ductility is attained by combining austenite and martensite in relatively simplistic mesostructures. This calls for further investigations into the strength difference and the topological distribution of constituents for effective exploitation in optimising the material's mechanical performance. This could be done by seeking more effective stress/strain distribution among phases or the maximisation of transformation-induced plasticity and other mechanisms such as twinning-induced plasticity that can result in, e.g., a better combination of strength and ductility or delayed material failure.

The application of localised laser treatments has been demonstrated to be an effective way of producing patterned structures in steel sheets and might be implemented in industrial lines. They can be applied in automobile and aircraft bodies, turbine blades or other thin components in multiple engineering applications and commodities. In this respect, further investigations should be carried out for adequate control of the microstructure by varying the laser parameters and by understanding the effect of flash heating on the transformation mechanisms and resulting microstructure features. Double-sided treatments will enable deeper penetration of laser-affected zones and straighter interfaces between different pattern constituents.

Other combinations of steel phases such as ferrite and martensite can be explored using, e.g., ferritic base microstructures and taking advantage of the self-quenching mechanism inherent in laser treatments. This approach could be also extended to other material families such as titanium alloys.

8. Conclusions

Austenite/martensite mesostructures have been created in a Fe-Ni-C steel by solid-state transformations using localised laser heat treatments in two martensitic base microstructures with distinct mechanical properties. The analysis of the microstructure and mechanical properties leads to the following conclusions:

- Laser affected zone, mainly consisting of austenite, penetrates to the whole thickness of 1 mm martensitic base specimens, enabling the creation of complex patterned mesostructured in many metal alloy applications using thin sheets.
- Pattern mesostructured steel properties can be modified by varying the martensite strength in the base microstructure and the *meso*-pattern at the gauge. In all the configurations, the UE of the lasered specimens is higher than that of the base martensitic microstructures. Clear differences in the strain partitioning, the hardening of different constituents and the failure of materials were observed depending on the strength difference between martensite and austenite and the topology.
- Hard martensite resulting from quenching seems to prevent austenite mechanically induced transformation more effectively than soft tempered martensite. However, increasing austenite stability is only partially responsible for achieving a high macroscopic uniform elongation, as a double laser line treatment over a tempered microstructure resulted in the highest uniform elongation in all composite materials. A high uniform elongation of the tempered martensite zone compared to reference tempered martensite explains the extended macroscopic uniform elongation in these conditions and suggests that the topology of the mesostructure is playing an important role in the deformation behaviour. Further investigations are ongoing to clarify the origin of these observations.
- The work hardening rates observed in the austenitic zones of the laser samples suggest that a surrounding quenched martensite base microstructure is more effective at preventing mechanically induced transformation. Higher work hardening rates observed in the specimens with a tempered base microstructure correspond to higher austenite decomposition for a given amount of strain.
- For the specimen-pattern combinations investigated in this work, total elongation in lasered specimens is particularly strongly influenced by the topology of the mesostructure for the tempered specimens. Whereas quenched base specimens behave similarly regardless of topology, T/A = shows a remarkable increase in UE and TE relative to T/A -, suggesting an important role for topology. Further assessment of this effect is ongoing. A possible explanation is that when austenite is fully decomposed in T/A composites, a new T/M composite is formed, whereas in M/A specimens they become monolithic M/M, i.e. base and freshly formed martensite exhibit similar properties.
- Some of the deformation mechanisms observed at the mesoscale resemble mechanisms reported in the literature for similar systems at the microscale. Hence, mesoscale systems can be used for a better understanding of microscale systems This understanding will enable a better design of hierarchical structures at multiple scales for tailoring the material's mechanical performance.

The concepts explored in this work can be extended to more complicated patterns and other base microstructures, which open novel strategies to engineer steel and other metal alloys.

Data availability

Data will be made available on request.

Declaration of Competing Interest

The authors declare that they have no known competing financial interests or personal relationships that could have appeared to influence the work reported in this paper.

Acknowledgements

The authors want to acknowledge J. van Slingerland and S. van Asperen from the Delft University of Technology, for their help and wise advice for the present work. They also acknowledge the devoted work of A.J. Bierens, P.P. van Houten H. Landwehr and J. A. Reijne which assisted in the realisation of experiments. The research leading to these results has received funding from the European Research Council under the European Union's Seventh Framework Programme (FP/2007–2013)/ERC Grant Agreement n. [306292].

References

[1] R.S. Lakes, T. Lee, A. Bersie, Y.C. Wang, Extreme damping in composite materials with negative-stiffness inclusions, Nature 410 (6828) (2001) 565–567, https://doi.org/10.1038/35069035.
[2] S. Bonfanti, R. Guerra, M. Zaiser, S. Zapperi, Digital strategies for structured and architected materials design, APL Mater. 9 (2) (2021) 020904, https://doi.org/10.1063/5.0026817.
[3] D. Mousanezhad, B. Haghpanah, R. Ghosh, A.M. Hamouda, H. Nayeb-Hashemi, A. Vaziri, Elastic properties of chiral, anti-chiral, and hierarchical honeycombs: A simple energy-based approach, Theor. Appl. Mech. Lett. 6 (2) (2016) 81–96, https://doi.org/10.1016/j.taml.2016.02.004.
[4] H. Jopek, T. Stręk, Thermoauxetic Behavior of Composite Structures, Materials (Basel) 11 (2018) 294, https://doi.org/10.3390/ma11020294.
[5] B. Xu, X. Huang, S.W. Zhou, Y.M. Xie, Concurrent topological design of composite thermoelastic macrostructure and microstructure with multi-phase material for maximum stiffness, Compos. Struct. 150 (2016) 84–102, https://doi.org/10.1016/j.compstruct.2016.04.038.
[6] D. Embury, O. Bouaziz, Steel-Based Composites: Driving Forces and Classifications, Annu. Rev. Mater. Res. 40 (1) (2010) 213–241, https://doi.org/10.1146/annurev-matsci-070909-104438.
[7] J.D. Verhoeven, A.H. Pendray, W.E. Dauksch, S.R. Wagstaff, Damascus Steel Revisited, JOM 70 (7) (2018) 1331–1336, https://doi.org/10.1007/s11837-018-2915-z.
[8] O. Bouaziz, Y. Bréchet, J.D. Embury, Heterogeneous and Architectured Materials: A Possible Strategy for Design of Structural Materials, Adv. Eng. Mater. 10 (1-2) (2008) 24–36, https://doi.org/10.1002/adem.200700289.
[9] M. Huang, C. Xu, G. Fan, E. Maawad, W. Gan, L. Geng, F. Lin, G. Tang, H. Wu, Y. Du, D. Li, K. Miao, T. Zhang, X. Yang, Y. Xia, G. Cao, H. Kang, T. Wang, T. Xiao, H. Xie, Role of layered structure in ductility improvement of layered Ti-Al metal composite, Acta Mater. 153 (2018) 235–249, https://doi.org/10.1016/j.actamat.2018.05.005.
[10] M. Ojima, J. Inoue, S. Nambu, P. Xu, K. Akita, H. Suzuki, T. Koseki, Stress partitioning behavior of multilayered steels during tensile deformation measured by in situ neutron diffraction, Scr. Mater. 66 (3-4) (2012) 139–142, https://doi.org/10.1016/j.scriptamat.2011.10.018.

[11] W.G. Moffatt, J. Wulff, Strength of silver brazed joints in mild steel, JOM 9 (4) (1957) 442–445, https://doi.org/10.1007/BF03397896.
[12] J.P. Oliveira, Z. Zeng, T. Omori, N. Zhou, R.M. Miranda, F.B. Fernandes, Improvement of damping properties in laser processed superelastic Cu-Al-Mn shape memory alloys, Mater. Des. 98 (2016) 280–284, https://doi.org/10.1016/j.matdes.2016.03.032.
[13] J.P. Oliveira, A.J. Cavaleiro, N. Schell, A. Stark, R.M. Miranda, J.L. Ocana, F.M. Braz Fernandes, Effects of laser processing on the transformation characteristics of NiTi: A contribute to additive manufacturing, Scripta Materialia 152 152 (2018) 122–126, https://doi.org/10.1016/j.scriptamat.2018.04.024.
[14] Z.-T. Zhao, X.-S. Wang, G.-Y. Qiao, S.-y. Zhang, B.o. Liao, F.-R. Xiao, Effect of bainite morphology on deformation compatibility of mesostructure in ferrite/bainite dual-phase steel: Mesostructure-based finite element analysis, Mater. Des. 180 (2019) 107870, https://doi.org/10.1016/j.matdes.2019.107870.
[15] L. Liu, Q. Yu, Z. Wang, J. Ell, M.X. Huang, R.O. Ritchie, Making ultrastrong steel tough by grain-boundary delamination, Science 368 (6497) (2020) 1347–1352.
[16] J. Mazumder, Laser Heat Treatment: The State of the Art, JOM 35 (5) (1983) 18–26, https://doi.org/10.1007/BF03338273.
[17] A.P. Mackwood, R.C. Crafer, Thermal modelling of laser welding and related processes: a literature review, Opt. Laser Technol. 37 (2) (2005) 99–115, https://doi.org/10.1016/j.optlastec.2004.02.017.
[18] B. Syed, S.M. Shariff, G. Padmanabham, S. Lenka, B. Bhattacharya, S. Kundu, Influence of laser surface hardened layer on mechanical properties of re-engineered low carbon steel sheet, Mater. Sci. Eng., A 685 (2017) 168–177, https://doi.org/10.1016/j.msea.2016.12.124.
[19] J. Leunda, V. García Navas, C. Soriano, C. Sanz, Effect of laser tempering of high alloy powder metallurgical tool steels after laser cladding, Surface and Coatings Technology 259 259 (2014) 570–576, https://doi.org/10.1016/j.surfcoat.2014.10.028.
[20] S.V. Telrandhe, J. Bhagyaraj, S. Mishra, S. Karagadde, A new approach to control and optimize the laser surface heat treatment of materials, J. Mater. Process. Technol. 262 (2018) 492–502, https://doi.org/10.1016/j.jmatprotec.2018.07.017.
[21] A.O. Andreev, D.P. Bykovskiy, A.V. Osintsev, V.N. Petrovskiy, I.I. Ryashko, E.N. Blinova, M.A. Libman, A.M. Glezer, Effect of the laser heat treatment on the formation of the gradient structures in alloys based on Fe – Cr – Ni system, J. Phys.: Conf. Ser. 941 (2017) 12027, https://doi.org/10.1088/1742-6596/941/1/012027.
[22] E.V. Pimenov, Possibilities of Using a Local Heat Treatment to Produce New Precision Alloys, Steel Transl. 49 (9) (2019) 649–651, https://doi.org/10.3103/S0967091219090109.
[23] J. Hidalgo, R.M. Huizenga, K.O. Findley, M.J. Santofimia, Interplay between metastable phases controls strength and ductility in steels, Mater. Sci. Eng., A 745 (2019) 185–194, https://doi.org/10.1016/j.msea.2018.12.096.
[24] S. Gates-Rector, T. Blanton, The Powder Diffraction File: a quality materials characterization database, Powder Diffr. 34 (4) (2019) 352–360, https://doi.org/10.1017/S0885715619000812.
[25] L. Lutterotti, M. Bortolotti, Object Oriented Programming and Fast Computation Techniques in MAUD, a Program for Powder Diffraction Analysis Written in, Java (2003).
[26] C.A. Schneider, W.S. Rasband, K.W. Eliceiri, NIH Image to ImageJ: 25 years of image analysis, Nat Methods 9 (7) (2012) 671–675, https://doi.org/10.1038/nmeth.2089.
[27] J. Pak, D.W. Suh, H.K.D.H. Bhadeshia, Displacive Phase Transformation and Surface Effects Associated with Confocal Laser Scanning Microscopy, Metall Mater Trans A 43 (12) (2012) 4520–4524, https://doi.org/10.1007/s11661-012-1264-8.
[28] Z. Tao, X.-Q. Wang, M.K. Hassan, T.-Y. Song, L.-A. Xie, Behaviour of three types of stainless steel after exposure to elevated temperatures, J. Constr. Steel Res. 152 (2019) 296–311, https://doi.org/10.1016/j.jcsr.2018.02.020.
[29] A.J. Goldman, W.D. Robertson, Elastic properties of austenite and martensite in iron-nickel alloys, Acta Metall. 12 (11) (1964) 1265–1275, https://doi.org/10.1016/0001-6160(64)90111-7.
[30] M. Yonemura, H. Nishibata, T. Nishiura, N. Ooura, Y. Yoshimoto, K. Fujiwara, K. Kawano, T. Terai, Y. Inubushi, I. Inoue, K. Tono, M. Yabashi, Fine microstructure formation in steel under ultrafast heating, Sci Rep 9 (2019) 11241, https://doi.org/10.1038/s41598-019-47668-6.
[31] B. Ahn, Recent Advances in Brazing Fillers for Joining of Dissimilar Materials, Metals 11 (2021) 1037, https://doi.org/10.3390/met11071037.
[32] M. Soleimani, A. Kalhor, H. Mirzadeh, Transformation-induced plasticity (TRIP) in advanced steels: A review, Mater. Sci. Eng., A 795 (2020) 140023, https://doi.org/10.1016/j.msea.2020.140023.
[33] P.J. Jacques, F. Delannay, J. Ladrière, On the influence of interactions between phases on the mechanical stability of retained austenite in transformation-induced plasticity multiphase steels, Metall. Mater. Trans. A 32 (11) (2001) 2759–2768, https://doi.org/10.1007/s11661-001-1027-4.